ORIGINAL ARTICLE

Journal Section

Assessment of a subgrid-scale model for convection-dominated mass transfer for initial transient rise of a bubble

A. Weiner[1] | **C.M.Y. Claassen**[2] | **I.R. Hierck**[2] | **J.A.M. Kuipers**[2] | **M.W. Baltussen**[2]

[1]TU Braunschweig, Institute of Fluid Mechanics, Hermann-Blenk-Str. 37, 38102 Braunschweig, Germany

[2]Multiphase Reactors Group, Department of Chemical Engineering and Chemistry, Eindhoven University of Technology, P.O. Box 513, 5612 AZ Eindhoven, The Netherlands

Correspondence
M.W.Baltussen, Department of Chemical Engineering and Chemistry, Eindhoven University of Technology, Eindhoven, P.O. Box 513, 5612 AZ, The Netherlands
Email: M.W.Baltussen@tue.nl

Funding information
Netherlands Organization for Scientific Research (NWO) TOP grant, Grant/Award Number: First principles based multi-scale modeling of transport in reactive three phase flows/716.014.001 and Netherlands Organization for Scientific Research (NWO) TOP grant, Grant/Award number: Reactive Gas-Liquid Two-Phase Flow in Porous Media/716.018.001.

The mass transfer between a rising bubble and the surrounding liquid is mainly determined by an extremely thin layer of dissolved gas forming at the liquid side of the gas-liquid interface. Resolving this concentration boundary layer in numerical simulations is computationally expensive. Subgrid-scale models mitigate the resolution requirements enormously and allow approximating the mass transfer in industrially relevant flow conditions with high accuracy. However, the development and validation of such models is difficult as only integral mass transfer data for steady-state conditions are available. Therefore, it is difficult to assess the validity of the sub-grid models in transient conditions. In this contribution, we compare the local and global mass transfer of an improved subgrid-scale model for rising bubbles ($Re = 72 - 569$ and $Sc = 10^2 - 10^4$) to a single-phase simulation approach, which maps the two-phase flow field to a highly-resolved mesh comprising only the liquid phase.

KEYWORDS
multiphase flows, mass transfer, high-Schmidt number problem, subgrid-scale modeling, machine learning

1 | INTRODUCTION

Many industrial processes are characterized as gas-liquid systems. A gas-liquid system is often favorable because of the good mass transfer characteristics. However, these mass transfer characteristics are difficult to determine. Thus, the optimization of the processes is challenging. Due to the typically high Schmidt and Reynolds numbers in gas-liquid systems, the species concentration boundary layer is very thin and hard to capture both experimentally and numerically. Nevertheless, the mass transfer in gas-liquid systems has been widely studied for decades. Some studies kept the Schmidt number relatively low to alleviate the resolution requirements [1,2,3,4]. Other studies used static local refinements with which they could simulate higher Schmidt numbers, however, only with a fixed bubble shape [5,6,7,8]. In the last decade the focus has been shifting to adaptive mesh refinement (AMR) techniques [9] and subgrid-scale (SGS) models [10,11,12,13,14,15,16]. Both approaches still have their challenges. In this work, we investigate the effectiveness of SGS models to simulate the mass transfer during the initial accelerated rise of small bubbles.

Two families of SGS models for computing the convection-dominated mass transfer at rising bubbles are available in literature. The first group [13,14,17] uses an analytical profile function or machine learning (ML) model to correct convective and diffusive species fluxes in cells containing or aligned with the gas-liquid interface. This type of SGS model has been implemented in volume-of-fluid [13,14] and interface-tracking [15,16] two-phase flow solvers. The second group [10,11,12] is more tailored to Front Tracking-based flow solvers. Instead of resolving the steep concentration profile in interface normal direction, the species mass contained in a fluid portion normal to the interface is stored on the front markers. As in the first group of SGS models, analytical profile functions are used to reconstruct the species distribution normal to the interface. Based on the profile, the profile's derivative can be evaluated at at a fixed distance away from the interface. Using this derivative, the mass exchange between gas and liquid and between bulk and boundary layer is computed. The SGS model presented in this contribution belongs to the latter group and is an improved version of the work by Claassen et al. [12]. This model is changed by enforcing the concentration at the end of the boundary layer to be equal to the concentration calculated by the SGS model. This is expected to be more accurate than specifying the mass flux at the end of the boundary layer. For a more detailed comparison of both SGS modeling approaches and an overview of other approaches to overcome the high-Schmidt number problem, the reader is referred to [18] and the references therein.

The challenge for SGS model development lies in the validation. The most straightforward approach to validate such a model would be to compare results for selected canonical cases against direct, fully resolved solutions. However, resolving the flow dynamics of a single rising bubble requires easily several weeks on a high-performance cluster. Since the species boundary layer thickness scales roughly with $Sc^{-1/2}$ compared to that of the momentum boundary layer around a clean interface, a 10-100 times denser mesh would be required for a direct solution of the species boundary layer. Moreover, the portions of the boundary layer that are the hardest to resolve typically have a fairly simple structure such that a direct solution of the full problem, two-phase flow and species transport, would yield little qualitative information.

Further reference data for validation is available from experiments and theoretical investigations. Both sources typically provide integral data like rise velocity or global Sherwood number. Local boundary layer data like species concentration fields are even harder to obtain in experiments than in simulations, but ultimately, it is necessary to show that the SGS model computes accurate local species transfer. Moreover, reference data is often only available for steady flow conditions, but those conditions do not reflect the ones encountered in bubble swarms.

Our approach to obtaining transient local reference data is as follows: first, the two-phase flow problem is solved; then, a single-phase simulation with fully resolved momentum and species transport in the liquid phase is computed. Machine learning models are used to map shape and velocity information from the two-phase to the single-phase

simulation to obtain accurate flow and species fields. This hybrid approach was first presented in Weiner et al.[18] for steady flow conditions and is here extended to the transient case.

The remainder of this article is structured as follows. In the next section, both approaches, the SGS model and the single-phase simulation approach, are described in more detail. Then, the mesh dependency is assessed for the highest investigated Reynolds, $Re = U_b d_b / \nu_l = 569$, and several Schmidt numbers, $Sc = D/\nu_l$ (U_b - terminal bubble velocity, d_b - equivalent bubble diameter, ν_l - kinematic liquid viscosity, D - molecular species diffusivity in the liquid phase). In the results section 4, we compare the time-dependent velocity and concentration fields as well as local and global mass transfer between both approaches for the ranges $Re = 72 - 569$ and $Sc = 10^2 - 10^4$. Finally, we discuss several possible points for improvements in both methods and suggest further investigations towards the simulation of bubbles undergoing path and shape oscillations.

The scientific data, scripts for data processing, analysis, and plotting, the source code and test cases of the single-phase approximation approach, as well as additional documentation are available via the Github repository[1] accompanying this article. Except for the two-phase flow simulations, which were performed on a high-performance cluster, all results were obtained in a fully reproducible manner using *Docker* software containers (instructions provided in the repository). Visualizations were created with *ParaView*[19] and *Matplotlib*[20]. The data processing was mostly implemented in *Numpy*[21] and *Pandas*[22]. The machine learning models for the single-phase simulation approach were created with *PyTorch*[23].

2 | NUMERICAL METHODS AND SETUPS

2.1 | Front Tracking

In this work, the used Front Tracking method is based on the method by van Sint Annaland et. al.[24], Dijkhuizen et al.[25] and Roghair et al.[26]. The implementation of the SGS model is an improved version of the SGS model of Claassen et al.[12]. In this paper, we will focus only on the main characteristics of the Front Tracking and the SGS model.

2.1.1 | Flow dynamics

The Front Tracking model solves the continuity equation, equation 1, and the Navier-Stokes equations, equation 2, for incompressible flows using a one-fluid approximation.

$$\nabla \cdot \mathbf{u} = 0 \tag{1}$$

$$\rho \frac{\partial \mathbf{u}}{\partial t} = -\nabla p - \rho \nabla \cdot (\mathbf{u}\mathbf{u}) - \nabla \cdot \mu \left[\nabla \mathbf{u} + (\nabla \mathbf{u})^T \right] + \rho \mathbf{g} + \mathbf{F}_\sigma \tag{2}$$

where $\mathbf{u}$ denotes the velocity vector, ρ the density, p the pressure, μ the viscosity, $\mathbf{g}$ the gravity vector and $\mathbf{F}_\sigma$ the surface tension force density vector relating the two phases. The density and viscosity are calculated on the fraction of liquid and gas in a cell in the previous time step using normal and harmonic averaging, respectively. The extra force density F_σ is directly calculated from the triangular mesh, which represents the gas-liquid interface. The force density

[1] https://github.com/AndreWeiner/sgs_model_test_transient

is determined by summing the tensile force on a marker, m, of adjacent markers as given in equation 3, which uses the joined tangent of the marker, $\mathbf{t}_{m,i}$, and the normal vector of the adjacent marker $\mathbf{n}_i$ [27].

$$\mathbf{F}_{\sigma,m} = \frac{1}{2}\sum_{i=1}^{3}\sigma\left(\mathbf{t}_{m,i}\times\mathbf{n}_i\right) \tag{3}$$

where σ is the surface tension coefficient. This tensile force of each marker is mapped to the surrounding Eulerian grid cells using mass-weighing [28]. However, this local mapping results in a mismatch in the discrete representation of the pressure and the surface tension, which leads to undesirable spurious currents. Therefore, a pressure-jump correction is implemented [29,30,25].

The velocity and pressure fields are solved using the projection-correction method on a staggered grid. All terms in the Navier-Stokes equations are treated explicitly, except for the viscous term, which is treated semi-implicitly. In the viscous terms, the implicit part is chosen such that all the velocity components can be solved separately. The viscous term and the convective term are discretized using the second order central differencing scheme and the second order flux-delimited Barton scheme, respectively. The implicit part of the viscous terms and the pressure correction are solved using a Block ICCG matrix solver.

After calculation of the velocity field, the bubble interface can be updated. The location of the Lagragian points, which form the triangulated grid, are advected with the local velocity using a fourth order Runga-Kutta method. The velocity is interpolated to the mesh using third order splines. Because the points are advected separately, the bubble interface is able to deform. This separate advection will lead to a decrease in the quality of the triangular mesh. To improve the mesh quality, three different remeshing operations have been implemented: edge splitting, edge collapsing and edge swapping [31,27]. Besides these remeshing operations, the smoothing algorithm of Kuprat et. al. [32] is included in the code to ensure a more even distribution of the points over the surface. Finally, the advection and the remeshing of the interface might lead to small volume errors, which are significant over a large number of time steps. These volume errors are corrected by redistribution of the lost (or gained) volume over all the points by moving them in the normal direction [33]. When the new interface location is known, the new local phase fraction of each cell can be computed geometrically.

2.1.2 | Mass transfer and the subgrid-scale model

In the bulk region, i.e. far away from the gas-liquid interface, the magnitude of the gradients in the species concentration, c, is expected to be relatively low, while near the gas-liquid interface high gradients are expected. Therefore, the bulk region and the region near the gas-liquid interface are treated differently.

For both regions, the distribution of species in the domain can be determined using the following equation:

$$\frac{\partial c}{\partial t} + (\mathbf{u}\cdot\nabla)c = D\nabla^2 c \tag{4}$$

Due to the low gradients in the bulk region, equation 4 can be determined on a relatively coarse grid. Therefore, the hydrodynamics grid will be used in the bulk region. The convection in the bulk region is discretized explicitly using a van Leer scheme, while the diffusion term is treated implicitly using a second order central differencing scheme.

The concentration gradients in the region near the gas-liquid interface are too large to be be resolved on the coarse hydrodynamics grid. Therefore, the concentration gradients in this region are approximated by a simplified

version of equation 4 according to the approach of Aboulhasanzadeh et al.[10]. The simplified advection-diffusion equation is solved for all the triangular markers of the interface. The used approximation of the concentration in the boundary layer is given by:

$$\frac{dc}{dt} = n\gamma\frac{\partial c}{\partial n} + D\frac{\partial^2 c}{\partial n^2}\text{, where } \gamma = -\frac{\partial u_n}{\partial n}. \tag{5}$$

In this equation n is the normal direction and γ is the strain rate. The equation assumes that the mass boundary layer is only affected by the compression (or expansion) of the surface and the diffusion in the normal direction. It is thus assumed that the concentration of each triangular marker is only affected in the normal direction of the bubble surface, i.e. all effects in the tangential direction and all effects due to curvature are neglected in the approximation. It should be noted that the tangential convection of the mass is included via the movement of the markers over the surface.

Using equation 5, the mass in the boundary layer of each marker can be determined via integration $M_0 = \int_0^{\delta_0} c(n)\,dn$, where δ_0 is a predefined maximum thickness in which the boundary layer model is used. In the model, the total mass per marker is determined by integration of equation 5.

$$\frac{dM_0}{dt} = -\gamma M_0 - D\left.\frac{\partial c}{\partial n}\right|_0 + \gamma c_{\delta_0}\delta_0 + D\left.\frac{\partial c}{\partial n}\right|_{\delta_0} \tag{6}$$

When the approximated mass boundary layer exceeds a predefined thickness δ_0, Aboulhasanzadeh et al.[10,11] transferred the last two terms to the bulk grid. In the current implementation, the concentration at δ_0 is enforced at the mass transfer grid using an approach similar to the Immersed Boundary method of Deen et al.[34]. This concentration can only be determined when the concentration profile is assumed. In this work, we will use the following profile for the concentration:

$$\frac{c(n)}{c_0} = \operatorname{erfc}\left(\sqrt{\pi}\frac{n}{\delta}\right) \tag{7}$$

Besides the changes due to diffusion and convection, the mass on a triangular marker can be changed due to the remeshing procedures described in the previous subsection. These changes in mass are treated as discussed in Claassen et al.[12].

| Sherwood number

The global and local Sherwood numbers are determined to enable a direct comparison between the two numerical methods. To calculate the global Sherwood number based on the effective transfer area $A_{eff} = \sum_{m\in M} A_m$ in the SGS model approach, the following equation is used:

$$Sh_{eff} = \frac{d_{eq}}{c_0 - c_\infty}\frac{\sum_{m\in M}\left.\frac{dc}{dn}\right|_{0,m} A_m}{\sum_{m\in M} A_m} \tag{8}$$

In this equation, the Sherwood number is based on the sphere-equivalent diameter, d_{eq}, M is the total set of all markers and A_m the area of marker m. The far field concentration c_∞ is zero in all cases considered here.

The local Sherwood number is calculated similarly to the global Sherwood number as shown in equation 9. The difference is that in the calculation of the local Sherwood number only markers with their center of mass within the considered range of angles, $\vartheta \pm \frac{1}{2}\Delta_\vartheta$, are taken into account. This subset of markers is represented by M_ϑ. The angle of a marker is calculated with equation 10, in which $\mathbf{x}$ is the center of mass of a marker (subscript m) or bubble (subscript b) and $\mathbf{e}_y$ is the unit vector in rise direction. The used Δ_ϑ is equal to 2 degrees.

$$Sh_{loc}(\vartheta) = \frac{d_{eq}}{c_0 - c_\infty} \frac{\sum_{m \in M_\vartheta} \left.\frac{dc}{dn}\right|_{0,m} A_m}{\sum_{m \in M_\vartheta} A_m} \tag{9}$$

$$\vartheta_m = cos\left(\frac{(\mathbf{x}_m - \mathbf{x}_b) \cdot \mathbf{e}_y}{|\mathbf{x}_m - \mathbf{x}_b|}\right) \tag{10}$$

2.1.3 | Simulation setup

In all the simulations, the bubbles are initialized as perfect spheres at the horizontal center of the domain and at 75% of the domain in the rise direction. A moving frame of reference[28] is used to keep the bubble center at this initial position. The used domain size is 6.25 bubble diameters in the rise direction and 4.7 bubble diameters in the horizontal direction. At all the domain boundaries a free-slip condition is applied for the velocity and a zero-gradient condition for the concentration. The used dimensionless time step, $\Delta\tilde{t}$, is 10^{-4}.

2.2 | Single-phase approximation

As the name suggests, the single-phase simulation approach is not a self-contained two-phase flow solver. Instead, two-phase flow and mass transfer are treated as two separate problems dealt with in two consecutive steps. This simplification allows computing directly resolved mass transfer at high Schmidt numbers in a short amount of time but it also introduces some limitations. For example, two-way interactions[15] between species transport and flow dynamics are difficult to implement. The basic idea is simple: first, a two-phase flow solution without species transport is computed to obtain the bubble's rise velocity, deformation, and interface velocity; then, the species transport problem is solved on a mesh containing only the liquid phase. Compared to the structured Cartesian mesh used for the two-phase flow simulations described in the previous section, the unstructured liquid-phase mesh used in the single-phase computations allows efficient placement of most cells close to the bubble's surface and wake. Moreover, the surface-aligned cell layers are suitable to resolve the strong gradients in the species concentration field. A further reduction of the computational costs is enabled by performing two-dimensional simulations. Axis-symmetry in azimuthal direction is assumed and implemented using OpenFOAM's wedge mesh approach[2].

2.2.1 | Flow dynamics

A divergence-free mapping of the velocity field from the two-phase to the single-phase domain is not straightforward. Instead, the flow solution is computed again on the unstructured single-phase mesh. To ensure that both velocity fields are as similar as possible, the boundary condition on the surface representing the bubble in the single-phase

[2] See section 4.2.2 of the OpenFOAM user guide for more information.

simulation must be chosen carefully. A typical approach would be to assume a free-slip condition, $\nabla \mathbf{u}|_s \cdot \mathbf{t}_s = 0$ and $\mathbf{u}_s \cdot \mathbf{n}_s$, where s denotes the bubble's surface as shown in figure 1. The surface normal vector $\mathbf{n}_s$ points into the liquid domain, and the tangential vector $\mathbf{t}_s$ is oriented as ϑ in figure 1. However, even for supposedly simple, almost spherical bubble shapes, a free-slip condition would introduce significant differences in the evolution of the flow and concentration fields. A provides more details and quantitative comparisons with the boundary condition outlined hereafter.

[Figure 1 about here.]

To compute a flow solution in the single-phase mesh that resembles its two-phase counterpart as closely as possible, the interface velocity is mapped from the two-phase flow field to the corresponding boundary in the single-phase simulation. First, the two-phase velocity is interpolated to the points located on the surface mesh, as indicated in figure 1. This interpolation is a standard operation in Front Tracking approaches. Details on the cubic spline interpolation can be found in Dijkhuizen et al.[35]. To obtain a 2D velocity profile, sector-wise averages along the circumference are computed, similar to those of the local Sherwood number. Neglecting any volume effects due to the mass transfer, the normal component of the velocity at the interface is zero in a reference frame moving with the bubble's center of mass. If $\mathbf{u}_\Sigma$ denotes the velocity vector at the interface Σ, then we assume $(\mathbf{u}_\Sigma - \mathbf{u}_b) \cdot \mathbf{n}_\Sigma = 0$. Note that the interface normal vector $\mathbf{n}_\Sigma$ is practically very close to but not exactly equal to $\mathbf{n}_s$ in the single-phase simulations. The remaining tangential velocity component is obtained by projecting the relative velocity onto the interface:

$$u_t = [\mathbf{u}_\Sigma - \mathbf{u}_b] \cdot \mathbf{t}_\Sigma. \tag{11}$$

The next step is to map u_t to the corresponding boundary in the single-phase simulation. Unfortunately, only a noisy estimate of $\mathbf{u}_\Sigma$ is known from the Front Tracking simulations, and the mapping has to be created by means of regression. Therefore, we train a simple multilayer perceptron (MLP) based on the discrete velocity information at the front points. The resulting machine learning model $\hat{u}_t(t, \vartheta)$ is a function of time t and polar angle ϑ. More details on the generic training of all machine learning models used in this work follow in the next section. Finally, the velocity vector at the boundary s in the single-phase simulation is computed as:

$$\mathbf{u}_s = \hat{u}_t(t, \vartheta)\mathbf{t}_s. \tag{12}$$

The moving reference frame formulation is necessary to keep the mesh deformation to a minimum. Since we consider the initial transient rise of the bubble, the inlet velocity in the single-phase simulations must be time-dependent, too. As for the interface velocity, we create a machine learning model $\hat{U}_b(t)$ for the bubble's terminal velocity $U_b = \mathbf{u}_b \cdot \mathbf{e}_y$, where $\mathbf{e}_y$ is the unit vector in rise direction. The inlet velocity vector $\mathbf{u}_{in}$ is then computed as:

$$\mathbf{u}_{in} = -\hat{U}_b(t)\mathbf{e}_y. \tag{13}$$

To consider shape deformation in the single-phase simulations, the boundary s must be moved over time, and the surrounding bulk mesh must deform accordingly to preserve mesh quality. Therefore, we parameterize the evolution of the interface as radius:

$$r(t, \vartheta) = |\mathbf{x}_\Sigma - \mathbf{x}_b|, \tag{14}$$

where $\mathbf{x}_b$ denotes the bubble's center of mass, and $\mathbf{x}_\Sigma$ is the position vector describing the interface. A machine learning model is trained based on the location of the front points and yields the approximation $\hat{r}(t,\vartheta) \approx r(t,\vartheta)$. In OpenFOAM, a Laplace equation for the mesh displacement $\Delta\mathbf{x}$ is solved to move the mesh points. At the boundary s, the displacement vector $\Delta\mathbf{x}_s$ is prescribed using the difference between the initial radius $r_0 = r(t=0,\vartheta) = 0.5d_b$ and the radius predicted for the current simulation time $\hat{r}(t,\vartheta)$:

$$\Delta\mathbf{x}_s = (\hat{r}(t,\vartheta) - r_0)\mathbf{e}_r, \tag{15}$$

where the unit vector in radial direction is defined as $\mathbf{e}_r = (\mathbf{x}_\Sigma - \mathbf{x}_b)/|\mathbf{x}_\Sigma - \mathbf{x}_b|$. At the wedge boundaries, no displacement normal to the boundary is allowed, and the displacement for all remaining boundaries is set to zero. To preserve the resolution in interface vicinity during mesh motion, a diffusion coefficient based on the quadratic inverse distance from the closest boundary is used in the Laplace equation for the displacement. For more information on the mesh motion, the reader is referred to Jasak and Tukovic[36].

Finally, to obtain the velocity field, the incompressible, isothermal Navier-Stokes equations are solved using the *pimpleFoam* solver. The pressure-velocity coupling at each time step is stopped once a tolerance of 10^{-4} is reached, which usually happens within two to three iterations. The time step varies between $\Delta\tilde{t} = 10^{-4}$ for test case CB4 and $\Delta\tilde{t} = 5\times10^{-5}$ for test case CB1 (at refinement level one; see section 3.2).

2.2.2 | Machine learning models

For readers without previous experience in machine learning, we recommend chapter 4 of reference[37] for a brief introduction tailored to the present work. We use MLPs (vanilla neural networks), the simplest type of neural network, for all required function approximations. All networks consist of two hidden layers with 40 neurons per layer and SELU activation functions[38]. This simple architecture is sufficient to obtain accurate function approximations for all cases investigated here. Note that the network architecture could be optimized in terms of free parameters for each individual model. However, the gain in terms of inference speed would be marginal. Moreover, evaluating the models during the simulation takes up a negligible amount of time.

The number of neurons in input and output layers varies according to the number of independent variables of the approximated function. All models depend on t. The models for radius and interface velocity also depend on the polar angle ϑ. The radius model is created in two steps for improved accuracy. First, the aspect ratio of the bubble's shape idealized as an ellipsoid is learned as a function of time. Then, a second model learns the deviation of the actual shape from the idealized ellipsoid. The model of the aspect ratio has two output neurons, one for each half-axis. All other models have only one output.

A mean squared error is used as loss function to adjust the models' weights. The weight update is computed using the ADAM optimizer[39]. Before the training, all inputs and outputs are scaled to the range $[0,1]$. The models are trained for 5000 to 20000 epochs, depending on the non-linearity of the approximated function, and the weights resulting in the lowest loss are kept for the final model. Since the mappings are low-dimensional and the relative amount of training data is large, no cross-validation was performed. For more details, the reader is referred to the accompanying code repository.

2.2.3 | Species transfer and transport

As in the Front Tracking approach, the species concentration field is obtained by solving equation 4. At the boundary of the bubble s, the concentration is set to unity and remains constant over time. At the outlet boundary, the concentration gradient is set to zero. At the inlet and side boundary, the concentration is set to zero. An implicit first-order Euler scheme is used to discretize in time. Diffusive fluxes are approximated by means of linear interpolation. The convective term is discretized using OpenFOAM's *linearUpwind* scheme, which switches between linear and upwind interpolation. Further details on the simulation setup are available in the accompanying code repository.

Once the concentration field is computed, time-dependent local and global mass transfer properties can be evaluated. The local Sherwood number is defined as:

$$Sh_{loc} = \frac{\nabla c|_s \cdot \mathbf{n}_s d_{eq}}{c_s - c_\infty}. \tag{16}$$

The far field concentration c_∞ is zero in all cases considered here. The global Sherwood number based on the effective transfer area A_{eff} is obtained by integrating the local Sherwood number over the bubble's surface. In the discrete sense, the integral becomes the following sum over all N_s faces on s:

$$Sh_{eff} = \sum_{i=1}^{N_s} Sh_{loc,i} A_i / \sum_{i=1}^{N_s} A_i, \tag{17}$$

where A_i is the face area of face i. In contrast to expression 17, correlations and experimental results are usually normalized using the sphere-equivalent surface area A_{eq}. The connection between effective and equivalent Sherwood number is given by the ratio of effective to equivalent surface area:

$$Sh_{eq} = Sh_{eff} \frac{A_{eff}}{A_{eq}}. \tag{18}$$

2.3 | Physical simulation parameters

The Morton number $Mo = g\mu_l^4/\rho_l/\sigma^3 = 2.57 \times 10^{-11}$ is the same for all cases and corresponds to an air-water system ($\log(Mo) = -10.59$, μ_l - dynamic liquid viscosity). The ratios between liquid and gas density and viscosity are $\rho_l/\rho_g = 100$ and $\mu_l/\mu_g = 100$. Note that the density ratio is decreased by a factor of ten compared to a physical gas-liquid system. The Eötvös or Bond number completes the case description and is defined as $Eo = g\rho_l d_b^2/\sigma$. Rising bubbles are also frequently characterized in terms of the Galilei number $Ga = \sqrt{g d_b^3}/\nu_l$, which we provide in addition to Eo in table 1.

[Table 1 about here.]

The diameters in table 1 have been selected such that the bubbles undergo a moderate deformation and rise on a straight path. The upper size limit at which small bubbles rising in pure water become path unstable is at roughly $d_b = 2mm$.

To simplify the parameter study and the analysis in terms of dimensionless numbers, gravity, equivalent bubble diameter, and liquid density are set to unity (in SI units) in all simulations. The Eötvös numbers according to table 1 are obtained by adjusting surface tension and dynamic viscosity as given in the second half of the table.

Regarding the species transport, three different Schmidt numbers $Sc = [100, 1000, 10000]$ are investigated. The resulting Péclet numbers, $Pe = ReSc$, vary between $Pe = 7.2 \times 10^3$ and $Pe = 5.7 \times 10^6$, and cover most of the industrially relevant parameter range.

3 | MESH DEPENDENCY STUDY

3.1 | Subgrid-scale model

The two-phase flow simulations employ an equidistant Cartesian mesh. Three different mesh resolutions have been investigated, which are reported in table 2.

[Table 2 about here.]

To reduce the overall number of simulations, the mesh dependency study has been performed only for case CB4, the case with the highest Reynolds number. Moreover, we only evaluate species transfer and transport quantities, namely the global and local Sherwood number as well as the wake concentration, and assume mesh independent flow dynamics if we find mesh independent species transport.

Besides the time-dependent equivalent global Sherwood number, figure 2 also depicts the frequently used correlation by Lochiel and Calderbank[40]:

$$Sh_{eq} = \frac{2}{\sqrt{\pi}} \left(1 - \frac{2.96}{\sqrt{Re}}\right)^{0.5} \sqrt{Pe}. \tag{19}$$

Equation 19 assumes a spherical shape, a steady state, as well as high Reynolds and Schmidt numbers to be most accurate. Compared to the numerical results on refinement levels one and two, equation 19 yields an about 7% smaller Sherwood number. All numerical results are in close agreement over the entire duration of the simulation. Note that we depict the time-dependent results over the characteristic time $\tilde{t} = t/\sqrt{g\, d_{eq}}$. The steady-state Sherwood number predicted on the coarsest mesh is about 5% smaller compared to the ones computed on the medium and fine meshes.

[Figure 2 about here.]

Also for the local Sherwood number, the SGS models delivers mostly mesh independent results for all investigated Schmidt numbers. This statement holds true for the temporal evolution of the local mass transfer, too.

[Figure 3 about here.]

The SGS model only corrects the species transport in the concentration boundary layer. Once the mass is released into the bulk mesh, convective and diffusive fluxes are computed based on the default interpolation scheme. Therefore, it is not surprising that the wake concentration in figure 4 shows a clear mesh dependency. The coordinate y_Σ is aligned with the y-axis but starts at the bubble's south pole. The deviation is more pronounced with increasing Schmidt number, which is not surprising since the characteristic spatial scales in the concentration field l_c scale approximately with $l_c \sim 1/\sqrt{Sc}$. Nonetheless, the qualitative behavior of the results on both meshes is comparable.

[Figure 4 about here.]

Based on these results, we consider refinement level one to be sufficiently mesh independent, at least with respect to the Sherwood numbers. Therefore, refinement level one is used for all remaining simulations. The simulations were performed on eight cores on a high performance cluster with $3.2GHz$ clock rate, and took between 5d18h (CB1 - Sc=10^2) and 5d6h (CB4 - Sc=10^3) to compute one dimensionless time unit. For comparison, the refinement levels zero and two simulations of CB4 at $Sc = 10^3$ required about 21h and 10d18h for one time unit, respectively.

3.2 | Single-phase approximation

The block-structured meshes used in the single-phase simulations were created with *blockMesh*. Most cells are concentrated around the surface boundary. To create a refined mesh, the number of cells in each direction of each block is doubled, but all other parameters, like cell expansion ratios, are kept constant. As a result, the width of the first cell layer Δ_1 along the boundary s is halved with each additional refinement level, and the overall number of cells is roughly four times larger, as can be seen in table 3.

[Table 3 about here.]

The second column in table 3 indicates the resolution of a Cartesian mesh to reach a similar cell width near the interface. The resolution in the single-phase simulations is roughly two orders of magnitude higher than in the two-phase simulations. Even with a two-phase flow solver supporting locally adaptive mesh refinement, it would be highly challenging or even impossible to reach such mesh densities. The three refinement levels compared in this section are depicted in figure 5.

[Figure 5 about here.]

As before, we compare local and global Sherwood numbers as well as the species concentration in the wake for test case CB4 (highest Reynolds number). Figure 6 depicts the computed global Sherwood number over time. Except for the highest Schmidt number, the curves of all three meshes are visually indistinguishable. For $Sc = 10^4$, the results on the coarsest mesh deviate by about 8% from the ones computed on refinement level one. As expected, the deviation is the highest in the initial stage $\tilde{t} < 0.5$ since the concentration boundary layer is still developing. The results indicate that refinement level one might be sufficiently mesh independent.

[Figure 6 about here.]

Favorable compensation of errors can yield integral quantities that appear more accurate than they actually are. Therefore, we also look at the local Sherwood numbers. Figure 7 shows several snapshots computed on refinement levels one and two. As for the global Sherwood numbers, the results are in close agreement. Only for the highest Schmidt number, a small deviation is visible at the upper half of the bubble, where the concentration gradients are the strongest. Note that there are several outliers in the scatter plot, especially close to the bubble's north pole. These extreme values originate from the difficulty of evaluating the concentration gradient in cells with extremely large aspect ratios. The closer cells are to the axis of rotation, the more the cell topology deteriorates due to the wedge domain, and therefore, the computed species transfer is less accurate. This observation holds true for the wake region, too, but the species transfer there is close to zero. A true two-dimensional mesh could potentially yield better results. However, we evaluated the mass transfer close to the front, $\vartheta < 3rad$, and found a contribution of about 0.1% to the global Sherwood number.

[Figure 7 about here.]

For completeness, we also look at the wake concentration along the axis of rotation. Figure 8 shows no significant difference between the results obtained on refinement levels one and two. Note that the cell size increases in the downstream direction, which presumably causes the small visible shift at $\tilde{t} \approx 2$. An interesting observation is that the concentration profile is not always monotonously decreasing for $Sc = [1000, 10000]$. We explain this effect in section 4.3.

[Figure 8 about here.]

Based on these results, we consider refinement level one to be sufficiently mesh independent for all remaining simulations. The simulations were performed on a single core with $2.6GHz$ clock rate, and took between 14h (CB1) and 6h (CB4) to compute one dimensionless time unit. For comparison, the refinement level zero and two simulations of CB4 required about 50min and 1.4d for one time unit, respectively. The latter simulation was performed in parallel on two cores.

4 | RESULTS

4.1 | Rise velocity, aspect ratio, and flow fields

To determine whether the flow dynamics in the simulations are correct, rise velocity and aspect ratio obtained in the simulations are compared to well known correlations in literature. Table 4 shows that the obtained rise velocity is within the range of the correlations of both Mei et al.[41] and Tomiyama et al.[42].

The simulation conditions were chosen such that the bubble shapes range from almost spherical (CB1) to moderately ellipsoidal (CB4). The results reflect this deformation behavior very well, as can be seen in table 4. The obtained aspect ratios also agree favorably with the experimental results of Duineveld et. al.[43]. For the highest Reynolds number (CB4), the numerically predicted deformation is about 10% lower compared to the experimental data. In simulations, an increase in the mesh density typically yields stronger deformations in the investigated regime such that the agreement, presumably, could be even better. In addition, the experiments in Duineveld et al.[43] still have a small amount of surfactants, which will influence the bubble shape more for more deformable bubbles.

[Table 4 about here.]

Besides the check with the correlations, the velocity profiles in both simulations are compared for case CB4 in figure 9. The velocity profile is the same in the proximity of the bubble. However, small differences are obtained at large distances from the bubble due to a difference in resolution of the grid, type of boundary conditions used and the distance to the domain boundaries.

[Figure 9 about here.]

4.2 | Global and local mass transfer

Figure 10 shows the time-dependent global Sherwood number for all investigated test cases. The results were obtained at refinement level one in both approaches. A first look reveals that the agreement is extremely good over the entire investigated range of Reynolds and Schmidt numbers. The maximum deviation of 2.47% of the final steady-state Sherwood number occurs for test case CB3 (second highest Re) and $Sc = 100$. For most test cases, the difference is

below 2%. The remaining deviation might be attributed to modeling errors and small differences in the liquid-phase velocity field close to the interface.

From the figure it is clear that the agreement of all simulations with the literature correlation of Lochiel and Calderbank, equation 19, is best for test case CB2 regardless of the Schmidt number. This observation is sensible because most of the assumptions necessary to derive equation 19 hold true in this case: the Reynolds number is high but not too high to cause a significant shape deformation; in conjunction with the overall high Schmidt numbers investigated here, the thin boundary layer assumption is fulfilled the best. When using a lower Reynolds number (i.e. CB1), the velocity and concentration boundary layer are significantly thicker. In case CB1, it is expected that the differences between the correlation and the simulation decrease with increasing Schmidt number as the concentration boundary layer thickness decreases. On the other hand, as the Reynolds number increases (i.e. CB3 and CB4), the shape becomes more deformed, and the boundary layers' shape change. All steady-state Sherwood numbers and their relative differences can be found in the complementary material.

[Figure 10 about here.]

Figure 11 shows the local Sherwood number at select time instances during the early stage of the bubble's rise. In contrast to the scatter plots presented in section 3, the curves have been smoothed with a Gaussian filter to enable a better visual comparison. Again, the agreement between both approaches is satisfying throughout the temporal evolution. Some differences are visible at low polar angles, which are caused by the outliers present in the single-phase simulation approach. However, as discussed in section 3.2, the area around the caps contributes little to the overall species transport. Note that the local Sherwood number in the SGS model approach does not exactly reflect its global counterpart due to the averaging procedure in the circumferential direction. In other words, integrating the circumference-weighted local Sherwood number over the polar angle yields slightly higher global Sherwood numbers. The reason is that 3D simulations on Cartesian meshes are usually not perfectly symmetric along the azimuth. Nonetheless, the influence is too small to affect the qualitative discussion of figure 11.

[Figure 11 about here.]

4.3 | Concentration fields

The discussion of the concentration field, in particular in the wake, is complex due to the various physical and numerical effects and their parameter-dependent impact on the results. Therefore, we want to start this section by listing the main effects at play:

- convection: the species transport along the interface and also in the wake along the rise direction is dominated by convection
- diffusion: close to the bubble's surface the main transport mechanics are diffusion normal to the surface (on the liquid side) and convection along the surface; the equilibrium of convection and diffusion forms the boundary layer; diffusion also occurs in the wake but is less important due to the high Schmidt number
- numerical diffusion: if the concentration profile is not sufficiently well approximated by the interpolation scheme, convective fluxes are erroneous; the discretization error acts similar to physical diffusion, hence the naming
- approximation error in diffusive fluxes: similar to numerical diffusion, the interpolation error of the concentration gradients on cell faces causes numerically enhanced diffusive fluxes (in principal, the fluxes could be also mitigated, but for high Schmidt numbers, they are usually enhanced)

Due to the acceleration the bubble undergoes, the above mechanisms act with varying intensity over time. The time-dependency is important to understand the concentration fields and profiles depicted in figures 12 and 13, respectively.

Figure 12 shows that the evolution of the wake concentration is in good agreement for all depicted cases. The agreement is similarly good for all other cases not depicted in the figure. In comparison to the single-phase results, the wake in the SGS simulation evolves faster by a small extend. This difference arises mostly due to numerical diffusion. Moreover, the wake in the SGS simulations is wider. This effect is mostly caused by approximation errors of diffusive fluxes, which numerically enhance diffusive fluxes normal to the rise direction. The discretization errors are mitigated to a large extent in the boundary layer by the SGS model. In the single-phase approximation, the errors are reduced by extreme mesh densities. The wake resolution is about 40 times higher in horizontal and 4 times higher in rise direction compared to the SGS model simulations. Still, the two-phase simulation results are close to their single-phase counterpart, which indicates that the high Schmidt number problem is less severe in the bulk compared to the boundary layer.

[Figure 12 about here.]

In figure 13, we look at concentration profiles close to the centerline to enable a more quantitative comparison than in figure 12. As discussed in section 3.1, the wake concentration in the SGS model simulations is not sufficiently mesh-independent. Nonetheless, the concentration profiles follow the qualitative behavior of the single-phase simulations over the entire parameter range. It is also clearly visible that the agreement improves with decreasing Péclet number, where the resolution requirements are smaller. The profiles in the SGS simulations evolve faster in downstream direction, which was already discussed before.

An interesting observation is that for some curves with $Re \geq 430$ and $Sc \geq 1000$, the concentration is not always monotonously decreasing. The behavior is caused by the bubble's acceleration in the initial stage. At the very beginning of the simulation, the bubble is at rest, and only diffusion acts. A concentration layer forms quickly around the interface because no species is present in the bulk, and the concentration normal derivative at the interface is correspondingly high. Then, as the bubble accelerates, convection transports the species along the surface to the rear part of the bubble and into the wake. Note that this interpretation considers a reference frame moving with the bubble. In the two-phase simulations as well as in experiments, convection rather causes the species "to be left behind". At some point, convection becomes stronger than diffusion such that the boundary layer depletes. Also the global Sherwood numbers reflect this behavior showing an increase after roughly $\tilde{t} \approx 0.5$. Due to the depletion, less species is transported through the boundary layer into the wake. The wake concentration close to the bubble around this point in time is consequently lower than it was before. At the same time, concentration gradients in the wake decay because of physically and numerically induced diffusion. This non-monotonous wake profile is only observed if the Schmidt number is sufficiently high and the mesh is dense enough, because in these cases the regions of increased concentration persists long enough. In some sense, one could say that the wake concentration reflects the mass transfer's history masked by bulk diffusion.

The effect described before is not too surprising. When looking at comparable experiments with visualized concentration fields[16], similar events take place: first; the bubble forms at the orifice; while it forms, it also starts to dissolve; when the bubble detaches, it leaves a region rich in transfer species behind. Of course, the mechanism in the experiment becomes even more intricate due to the formation process.

[Figure 13 about here.]

Another observation in figure 13 is that the SGS model results are sometimes below and sometimes above the ones of the single-phase simulation. We attribute this observation to the varying error sources associated with the mesh dependency mentioned before. The discretization error varies with both Reynolds and Schmidt number. We omit a detailed discussion of each individual test case.

5 | SUMMARY AND OUTLOOK

In this contribution, we introduced improved versions of two approaches to compute the convection-dominated mass transfer from rising bubbles. The main finding is that the SGS model yields excellent mass transfer predictions for a wide range of relevant Reynolds and Schmidt numbers. This statement holds true for the steady rise as well as the initial stage, in which the bubble undergoes strong deformation and acceleration. The extended transient single-phase simulation approach approximates the two-phase velocity field extremely well and presents itself as an excellent validation tool. Of course, there are still several open questions and possible improvements in both methods. Regarding the transient mass transfer, little is known about the local mass transfer at dynamic bubbles undergoing path instability and shape oscillations at realistic Reynolds and Schmidt numbers. The present results suggest that the SGS model could perform well under such conditions, but a thorough validation would be necessary. If the SGS passes this challenging test, it could be applied with much higher confidence to even more complex tasks like bubble swarm simulations. Regarding the numerical methods, the single-phase simulation approach could be improved by building further mathematical constraints into the ML models. For example, fulfilling the symmetry boundary condition at the central axis of rotation exactly by definition could mitigate the outliers in the local mass transfer close to the poles. The SGS model currently assumes a species concentration of zero in the surrounding liquid bulk, which should be taken into account, for example, to simulate bubble-bubble interactions or systems with multiple species and chemical reactions. Moreover, the present implementation would not be ideal to approximate reactive boundary layers since the concentration profile function was derived assuming pure physisorption. Reactive boundary layers could be dealt with by replacing the present profile function with more complex ones or by using a ML model instead. The biggest open question is the SGS modeling in the liquid bulk. There have been only a few successful attempts towards tackling this problem.

6 | ACKNOWLEDGEMENT

This work is part of the research program ”First principles based multi-scale modeling of transport in reactive three phase flows” with project number 716.014.001, which is financed by the Netherlands Organization for Scientific Research (NWO) TOP grant. This work is also part of the research program “Reactive Gas-Liquid Two-Phase Flow in Porous Media”, with project number 716.018.001, which is financed by the Netherlands Organization for Scientific Research (NWO) TOP grant. Andre Weiner thankfully acknowledges the many years of guidance and support by Prof. Dieter Bothe, which formed the basis for this project.

A | SLIP BOUNDARY CONDITION AND STATIC SHAPE

This section aims to emphasize why the data-driven mapping of velocity and shape information from the two-phase to the single-phase simulation is essential. Performing approximate species transport simulations in single-phase settings

is not a new idea and has been performed in numerous studies. Typically, a free-slip boundary condition for the velocity is assumed at the boundary representing the bubble. The resulting steady-state mass transfer at moderately deformed ellipsoids is usually in good agreement with other references. However, for more complex shapes, the free-slip condition is not a suitable assumption, as has been reported in [37]. Moreover, the applicability in transient cases with shape deformation has not been investigated yet. A strong suit of the modular implementation in OpenFOAM is that we can switch off individual machine learning models and observe their effect on the results. Specifically, we investigate the following scenarios:

1. **hybrid**: full setup with models for rise velocity, interface velocity, and deformation
2. **slip**: models for rise velocity and deformation but free-slip boundary condition for the interface velocity
3. **static**: model for the rise velocity, no shape deformation, free-slip boundary condition for the interface velocity

As can be seen in figure 14, the transient behavior of the global Sherwood number starts to deviate after about $\tilde{t} \approx 0.5$ if the free-slip boundary condition is applied. In the steady-state, the simulation with mesh deformation and free-slip condition yields a 5% increased Sherwood number, whereas the static simulation results in a 5% lower value. The maximum deviation in the transient stage is about 13%. These observations are qualitatively independent of the Schmidt number.

[Figure 14 about here.]

The bubble's deformation to an ellipsoidal shape causes a flattening of the local Sherwood number for $\vartheta < 1.5$ and a strong decrease around the equator region; see figure 15. This behavior is present in both simulations including mesh deformation. As observed in the global Sherwood number, the slip condition results in an increased transfer rate. The setup with static shape and slip condition yields a curve similar to semi-analytical results from potential and Stokes flow. The mass transfer is higher than in the other curves in the front but then drops more quickly for polar angles associated with high circumference. Therefore, the integral Sherwood number is lower than in the other cases.

[Figure 15 about here.]

It is known that a slip boundary condition yields good results for flow dynamics and mass transfer in the steady-state of a rising bubble. However, figure 16 shows that the evolution of the concentration is not predicted well with the slip condition. In the steady-state, both results would appear visually similar, but in the initial transient state, the wake concentration advances much quicker with the approximated two-phase flow field. This result also indicates that the slip condition, presumably, will not yield good results for even more dynamic rise behaviors like bubbles undergoing path instability.

[Figure 16 about here.]

Finally, we look at the concentration along a line in the wake 17. Again, the wake concentration advances much quicker in the hybrid approach simulations. It is interesting to see that both simulations employing a slip condition evolve similarly. This observation indicates that the velocity boundary condition contributes most to the substantial deviation from the two-phase approximation rather than the shape deformation.

[Figure 17 about here.]

references

1 Onea A, Wörner M, Cacuci DG. A qualitative computational study of mass transfer in upward bubble train flow through square and rectangular mini-channels. Chemical Engineering Science 2009;64(7):1416–1435.

2 Alke A, Bothe D, Kroeger M, Warnecke HJ. VOF-based simulation of conjugate mass transfer from freely moving fluid particles. Computational Methods in Multiphase Flow V 2009;p. 157–168.

3 Darmana D, Deen NG, Kuipers JAM. Detailed 3D Modeling of Mass Transfer Processes in Two-Phase Flows with Dynamic Interfaces. Chemical Engineering & Technology 2006;29:1027–1033.

4 Roghair I, van Sint Annaland M, Kuipers JAM. An improved Front-Tracking technique for the simulation of mass transfer in dense bubbly flows. Chemical Engineering Science 2016;152:351–369.

5 Jung RT, Sato T. Direct Numerical Simulation on Single-Droplet Flow with Mass Transfer. Chem Eng Technol 2001;24:1071–1075.

6 Dani A, Cockx A, Guiraud P. Direct numerical simulation of mass transfer from spherical bubbles: the effect of interface contamination at low Reynolds numbers. International Journal of Chemical Reactor Engineering 2006;4:A2.

7 Wylock C, Larcy A, Colinet P, Cartage T, Haut B. Direct numerical simulation of bubble-liquid mass transfer coupled with chemical reactions: Influence of bubble shape and interface contamination. Colloids ans Surfaces A: Physicochem Eng Aspects 2011;381:130–138.

8 Colombet D, Legendre D, Cockx A, Guiraud P. Mass or heat transfer inside a spherical gas bubble at low to moderate Reynolds number. International Journal of Heat and Mass Transfer 2013;67:1096–1105.

9 Panda A, Peters EAJF, Baltussen MW, Kuipers JAM. Fully resolved scalar transport for high Prandtl number flows using adaptive mesh refinement. Chemical Engineering Science: X 2019 11;4.

10 Aboulhasanzadeh B, Thomas S, Taeibi-Rahni M, Tryggvason G. Multiscale computations of mass transfer from buoyant bubbles. Chemical Engineering Science 2012;75:456 – 467.

11 Aboulhasanzadeh B, Hosoda S, Tomiyama A, Tryggvason G. A validation of an embedded analytical description approach for the computations of high Schmidt number mass transfer from bubbles in liquids. Chemical Engineering Science 2013;101:165 – 174.

12 Claassen CMY, Islam S, Peters EAJFF, Deen NG, Kuipers JAMH, Baltussen MW. An improved subgrid scale model for front-tracking based simulations of mass transfer from bubbles. AIChE Journal 2020;66(4):e16889.

13 Bothe D, Fleckenstein S. A Volume-of-Fluid-based method for mass transfer processes at fluid particles. Chemical Engineering Science 2013;101:283–302.

14 Weiner A, Bothe D. Advanced subgrid-scale modeling for convection-dominated species transport at fluid interfaces with application to mass transfer from rising bubbles. Journal of Computational Physics 2017;347(1):261–289.

15 Pesci C, Weiner A, Marschall H, Bothe D. Computational analysis of single rising bubbles influenced by soluble surfactant. Journal of Fluid Mechanics 2018;856:709–763.

16 Weiner A, Timmermann J, Pesci C, Grewe J, Hoffmann M, Schlüter M, et al. Experimental and numerical investigation of reactive species transport around a small rising bubble. Chemical Engineering Science: X 2019;1:100007.

17 Weiner A, Hillenbrand D, Marschall H, Bothe D. Data-Driven Subgrid-Scale Modeling for Convection-Dominated Concentration Boundary Layers. Chemical Engineering & Technology 2019;42(7):1349–1356.

18 Weiner A, Gründing D, Bothe D. Computing Mass Transfer at Deformable Bubbles for High Schmidt Numbers. Chemie Ingenieur Technik 2021;93(1-2):81–90.

19 Ahrens JP, Geveci B, Law CC. ParaView: An End-User Tool for Large-Data Visualization. In: Hansen CD, Johnson CR, editors. The Visualization Handbook Academic Press / Elsevier; 2005.p. 717–731.

20 Hunter JD. Matplotlib: A 2D graphics environment. Computing in Science & Engineering 2007;9(3):90–95.

21 Harris CR, Millman KJ, van der Walt SJ, Gommers R, Virtanen P, Cournapeau D, et al. Array programming with NumPy. Nature 2020 Sep;585(7825):357–362.

22 Wes McKinney. Data Structures for Statistical Computing in Python. In: Stéfan van der Walt, Jarrod Millman, editors. Proceedings of the 9th Python in Science Conference; 2010. p. 56 – 61.

23 Paszke A, Gross S, Massa F, Lerer A, Bradbury J, Chanan G, et al. PyTorch: An Imperative Style, High-Performance Deep Learning Library. In: Wallach H, Larochelle H, Beygelzimer A, d'Alché-Buc F, Fox E, Garnett R, editors. Advances in Neural Information Processing Systems 32 Curran Associates, Inc.; 2019.p. 8024–8035. http://papers.neurips.cc/paper/9015-pytorch-an-imperative-style-high-performance-deep-learning-library.pdf.

24 van Sint Annaland M, Dijkhuizen W, Deen NG, Kuipers JAM. Numerical simulation of behavior of gas bubbles using a 3-D Front-Tracking method. AIChE Journal 2006;52:99–110.

25 Dijkhuizen W, Roghair I, van Sint Annaland M, Kuipers JAM. DNS of gas bubbles behaviour using an improved 3D Front Tracking model–Model development. Chemical Engineering Science 2010;65(4):1427–1437.

26 Roghair I, Lau YM, Deen NG, Slagter HM, Baltussen MW, van Sint Annaland M, et al. On the drag force of bubbles in bubble swarms at intermediate and high Reynolds numbers. Chemical Engineering Science 2011;66:3204–3211.

27 Tryggvason G, Bunner B, Esmaeeli A, Juric D, Al-Rawahi N, Tauber W, et al. A Front-Tracking Method for the Computations of Multiphase Flow. Journal of Computational Physics 2001;169(2):708–759.

28 Deen NG, van Sint Annaland M, Kuipers JAM. Multi-scale modeling of dispersed gas-liquid two-phase flow. Chemical Engineering Science 2004;59(8-9):1853–1861.

29 Renardy Y, Renardy M. PROST: A Parabolic Reconstruction of Surface Tension for the Volume-of-Fluid Method. Journal of Computational Physics 2002;183(2):400–421.

30 Francois MM, Cummins SJ, Dendy ED, Kothe DB, Sicilian JM, Williams MW. A balanced-force algorithm for continuous and sharp interfacial surface tension models within a volume tracking framework. Journal of Computational Physics 2006;213(1):141–173.

31 Unverdi SO, Tryggvason G. A Front-Tracking method for viscous, incompressible, multi-fluid flows. Journal of Computational Physics 1992;100(1):25–37.

32 Kuprat A, Khamayseh A, George D, Larkey L. Volume Conserving Smoothing for Piecewise Linear Curves, Surfaces, and Triple Lines. Journal of Computational Physics 2001;172:99–118.

33 Roghair I, Van Sint Annaland M, Kuipers JAM. An improved Front-Tracking technique for the simulation of mass transfer in dense bubbly flows. Chemical Engineering Science 2016;152:351–369.

34 Deen NG, Kriebitzsch SHL, van der Hoef MA, Kuipers JAM. Direct Numerical Simulation of flow and heat transfer in dense fluid-particle systems. Chemical Engineering Science 2012;81:329–344.

35 Dijkhuizen W. Deriving closures for bubbly flows using direct numerical simulations. PhD thesis, UT; 2008.

36 Jasak H, Tukovic Z. Automatic mesh motion for the unstructured finite volume method. Transactions of Famena 2007;30:1–20.

37 Weiner A. Modeling and simulation of convection-dominated species transfer at rising bubbles. PhD thesis, Technical University of Darmstadt, Mathematical Modeling and Analysis; 2020.

38 Klambauer G, Unterthiner T, Mayr A, Hochreiter S. Self-Normalizing Neural Networks. CoRR 2017;abs/1706.02515. http://arxiv.org/abs/1706.02515.

39 Kingma DP, Ba J, Adam: A Method for Stochastic Optimization; 2014.

40 Lochiel AC, Calderbank PH. Mass transfer in the continuos phase around axissymmetric bodies of revolution. Chemical Engineering Science 1964;19:471–484.

41 Mei R, Klausner JF, Lawrence CJ. A note on the history force on a spherical bubble at finite Reynolds number. Physics of Fluids 1994;6(1):418–420. https://doi.org/10.1063/1.868039.

42 Tomiyama A, Kataoka I, Zun I, Sakaguchi T. Drag Coefficients of Single Bubbles under Normal and Micro Gravity Conditions. JSME International Journal Series B 1998;41(2):472–479.

43 Duineveld PC. The rise velocity and shape of bubbles in pure water at high Reynolds number. Journal of Fluid Mechanics 1995;292:325–332.

1. two-phase flow solution

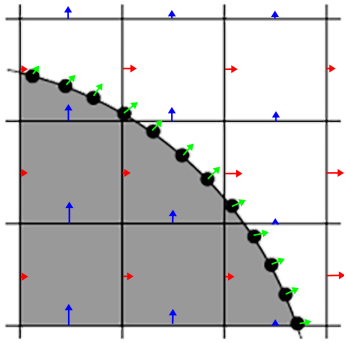

2. machine learning

rise velocity

$\hat{U}_b(t) \approx \mathbf{u}_b \cdot \mathbf{e}_y$

deformation

$\hat{r}(t,\vartheta) \approx |\mathbf{x}_\Sigma - \mathbf{x}_b|$

interface velocity

$\hat{u}_t(t,\vartheta) \approx [\mathbf{u}_\Sigma - \mathbf{u}_b] \cdot \mathbf{t}_\Sigma$

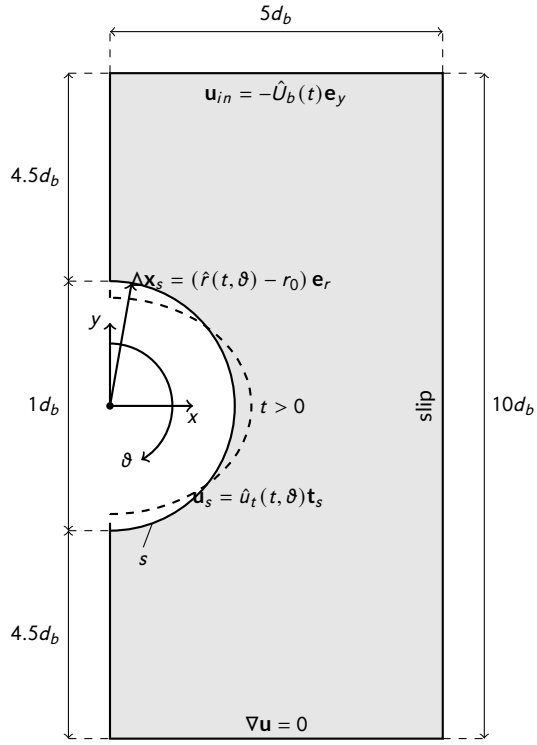

3. single-phase simulation

FIGURE 1 Single-phase simulation workflow and case setup.

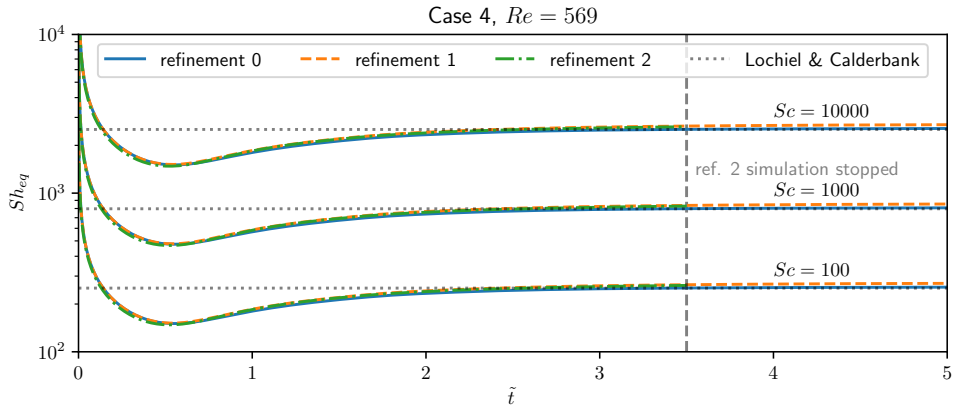

FIGURE 2 Global Sherwood number for test case 4 ($Re = 569$) computed on meshes according to table 2. The reference corresponds to equation 19.

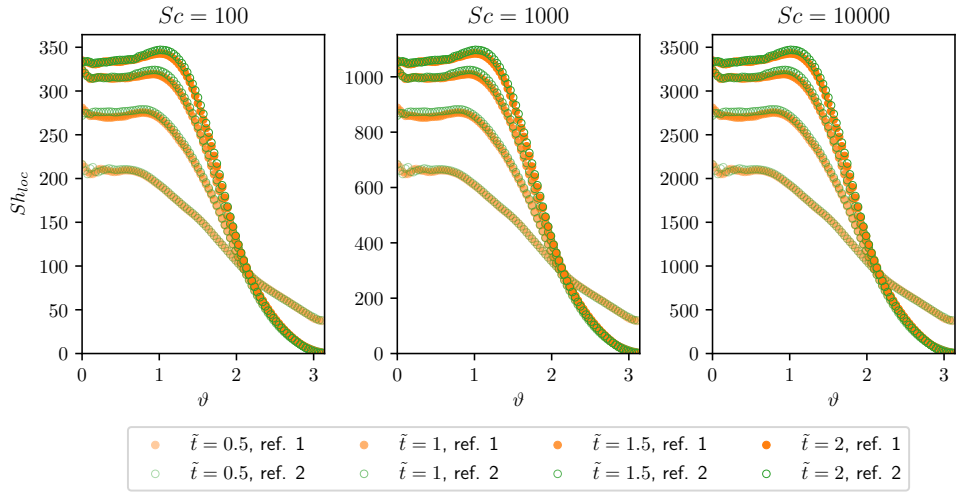

FIGURE 3 Local Sherwood number at selected time instances of test case 4 ($Re = 569$) computed on meshes 1 and 2 according to table 2.

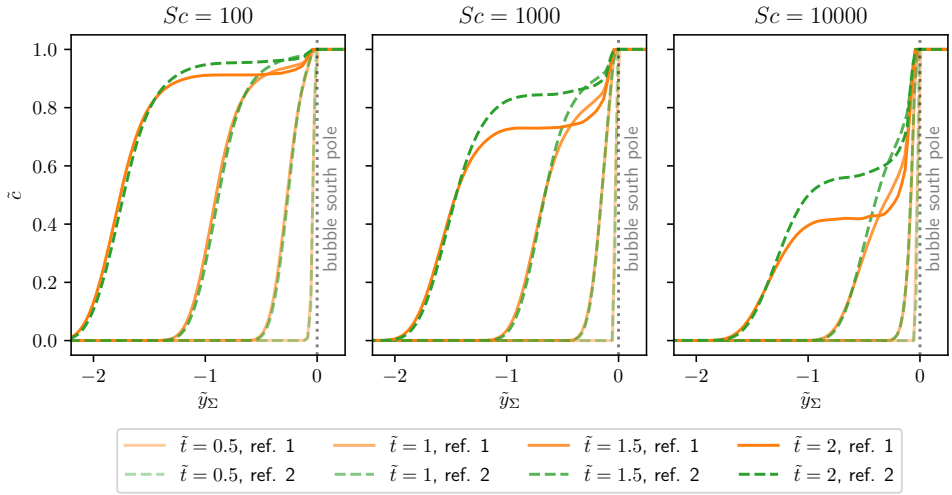

FIGURE 4 Wake concentration along the y-axis at selected time instances of test case 4 ($Re = 569$) computed on meshes 1 and 2 according to table 2.

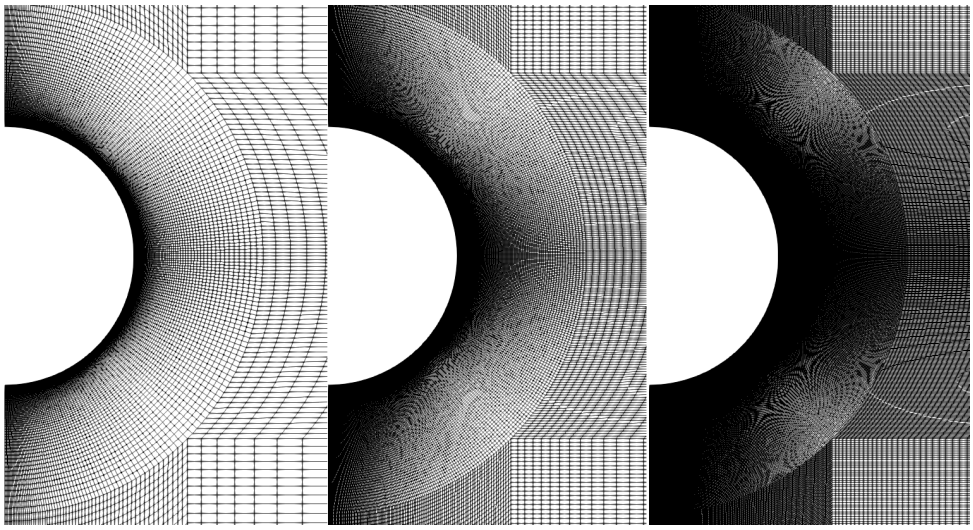

FIGURE 5 Coarse, medium, and fine mesh for the single-phase simulations corresponding to the properties in table 3.

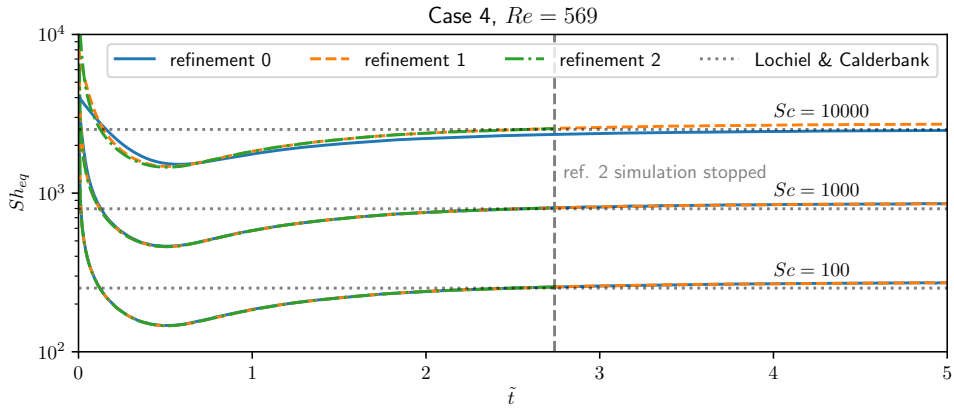

FIGURE 6 Global Sherwood number for test case 4 ($Re = 569$) computed on meshes according to table 3. The reference corresponds to correlation 19.

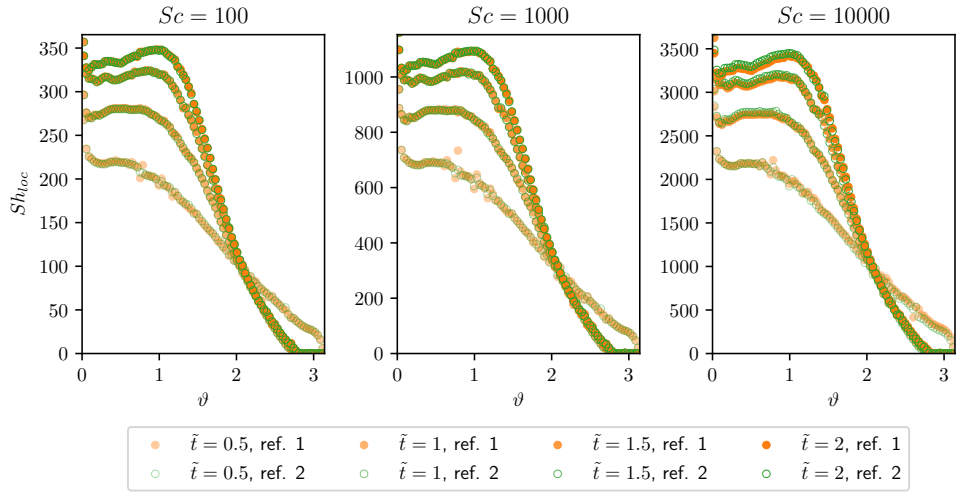

FIGURE 7 Local Sherwood number at selected time instances of test case 4 ($Re = 569$) computed on meshes 1 and 2 according to table 3.

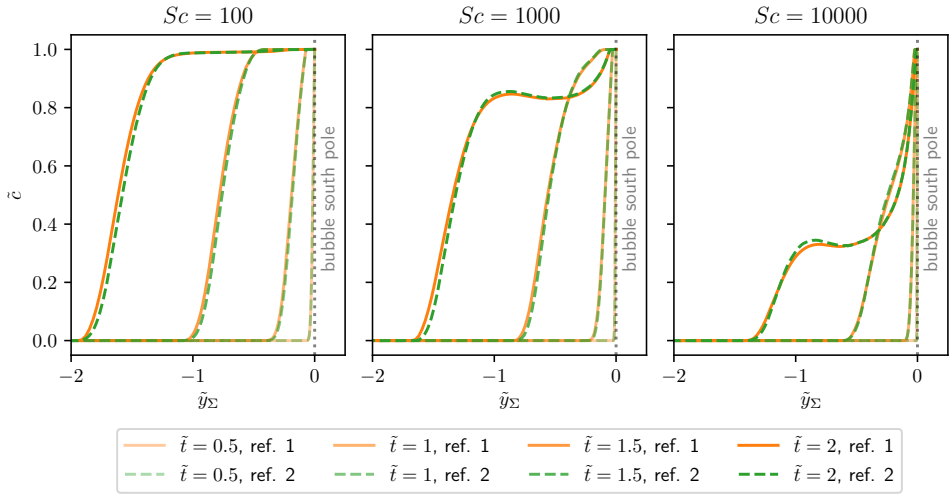

FIGURE 8 Wake concentration along the y-axis at selected time instances of test case 4 ($Re = 569$) computed on meshes 1 and 2 according to table 3.

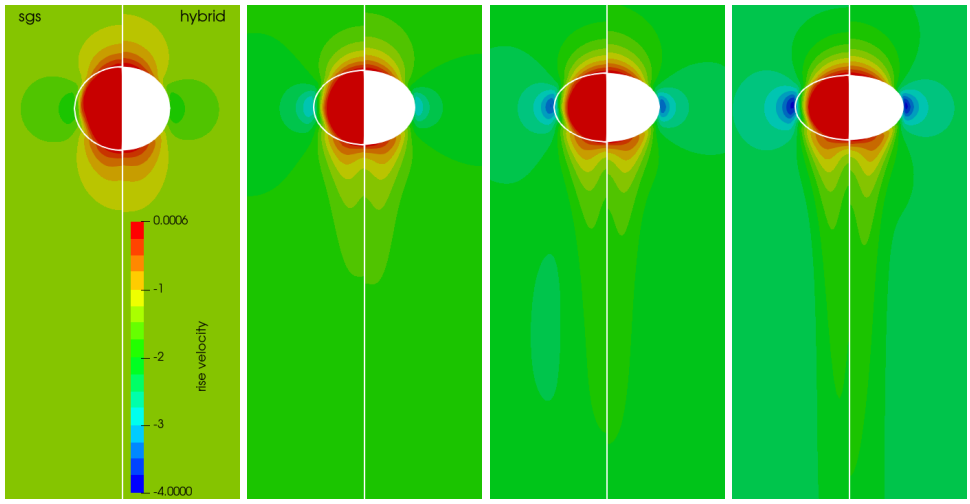

(a) $\tilde{t} = 1$ (b) $\tilde{t} = 2$ (c) $\tilde{t} = 3$ (d) $\tilde{t} = 5$

FIGURE 9 Rise velocity field at different times for the highest Reynolds number case (CB4).

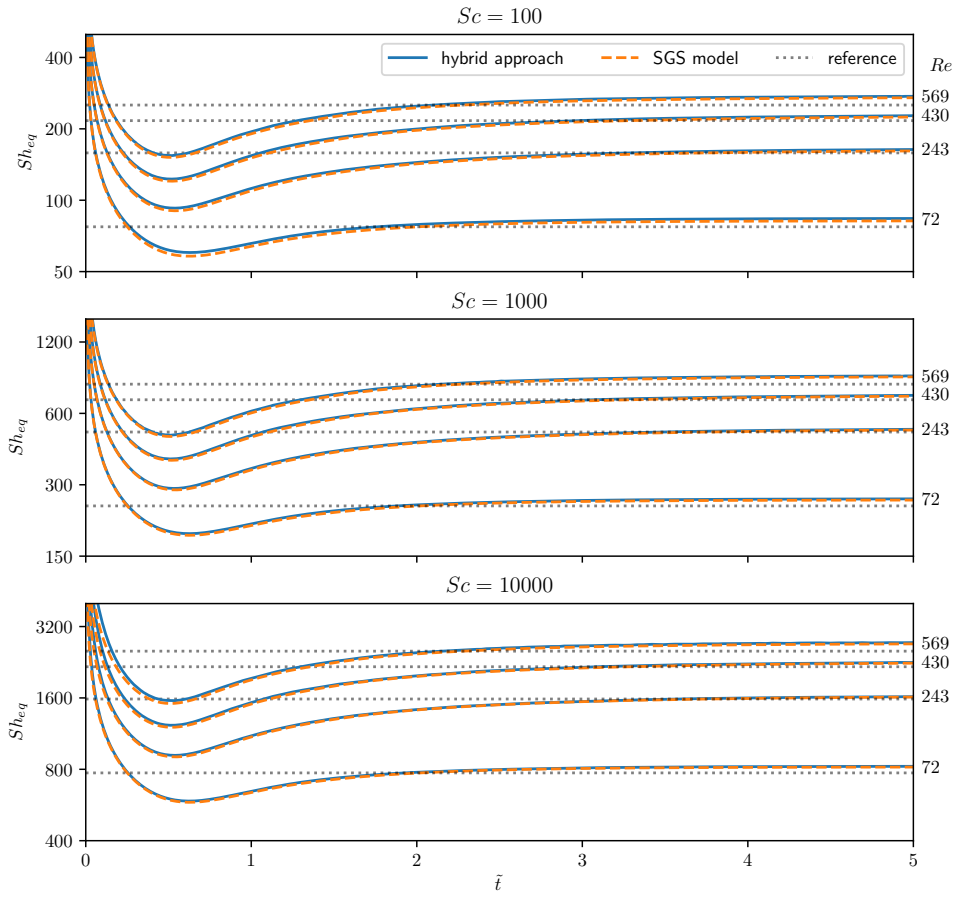

FIGURE 10 Comparison of the equivalent global Sherwood number's temporal evolution computed with hybrid approach and SGS model. The reference corresponds to Lochiel's correlation, eq. 19.

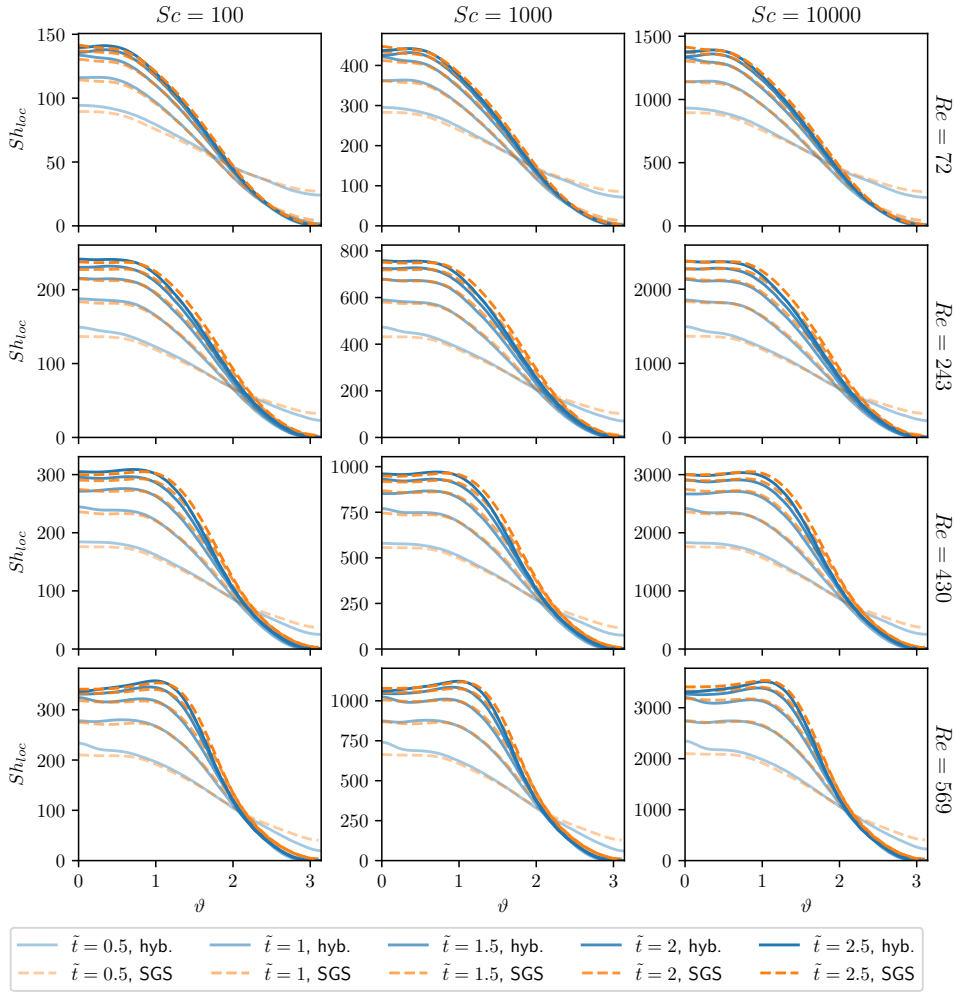

FIGURE 11 Comparison of the local Sherwood number at selected time instances during the transient phase computed with hybrid approach and SGS model.

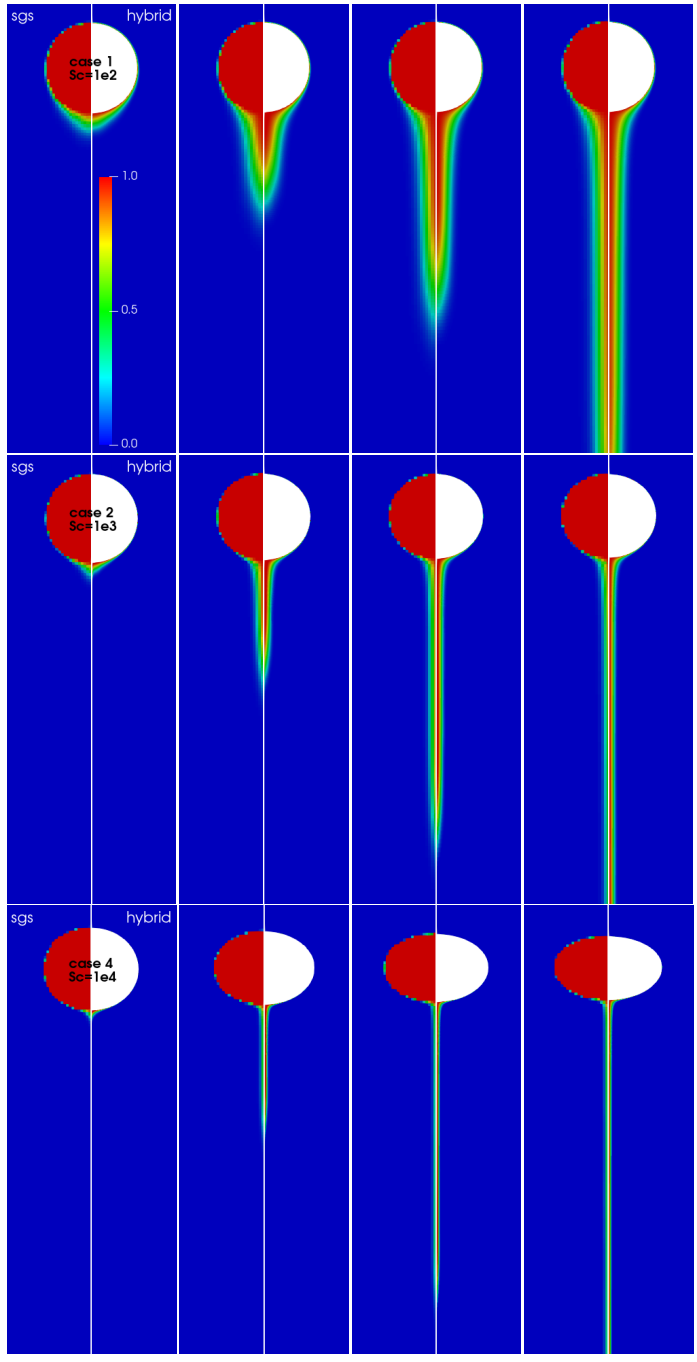

(a) $\tilde{t} = 1$ (b) $\tilde{t} = 2$ (c) $\tilde{t} = 3$ (d) $\tilde{t} = 5$

FIGURE 12 Concentration field at different times for the lowest Reynolds and Schmidt number case (top), case CB2 (middle) and the highest Reynolds and Schmidt number case (bottom).

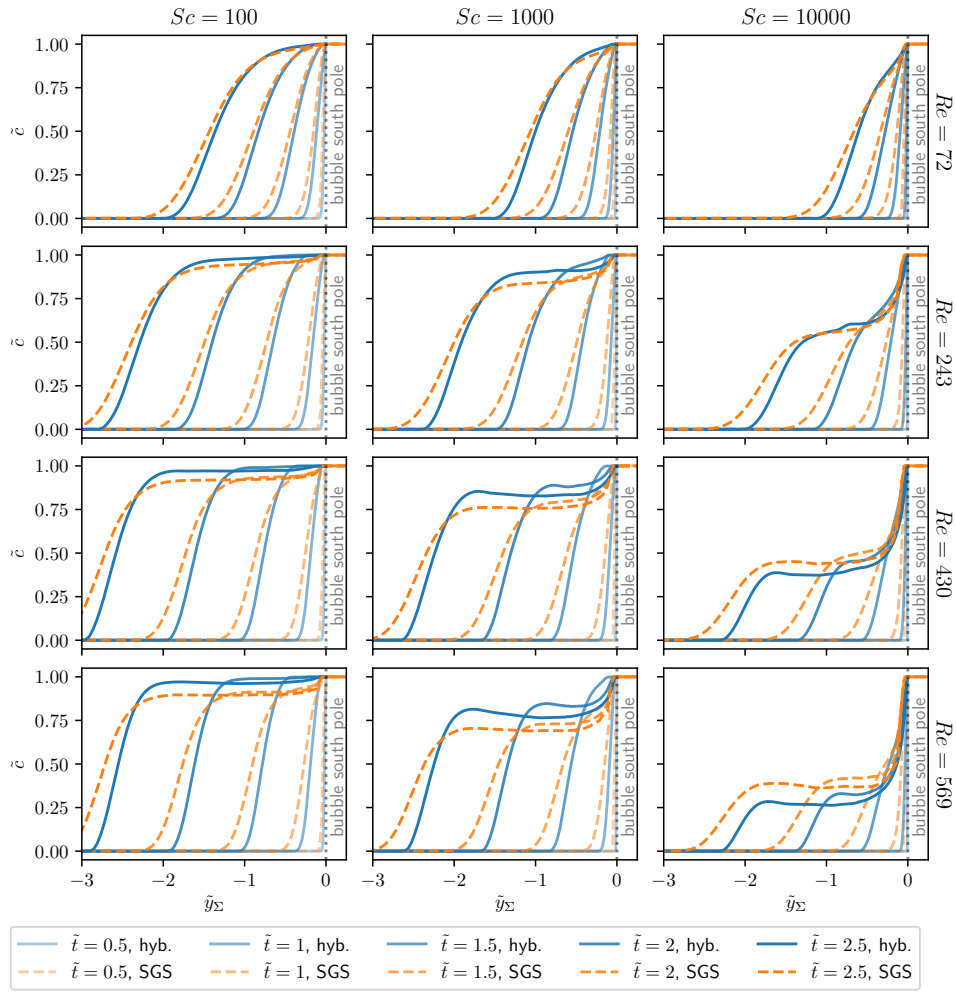

FIGURE 13 Comparison of the wake concentration along a line in y-direction.

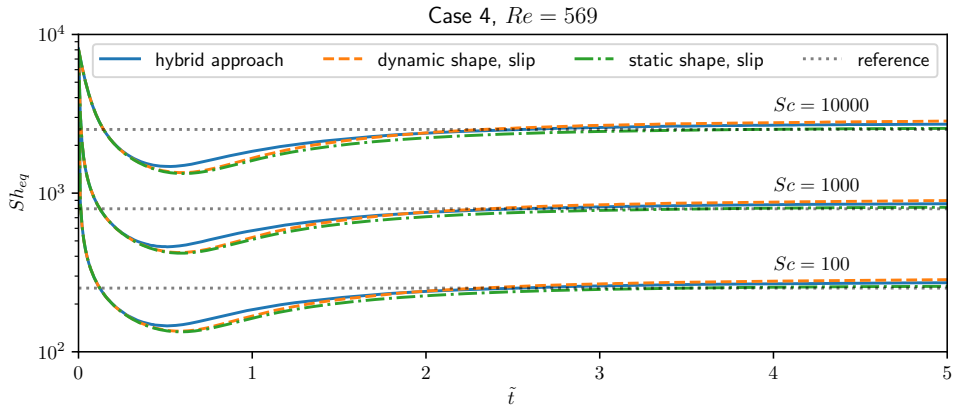

FIGURE 14 Global Sherwood number for test case 4 ($Re = 569$) computed with alternative boundary conditions. The reference corresponds to Lochiel's correlation, eq. 19.

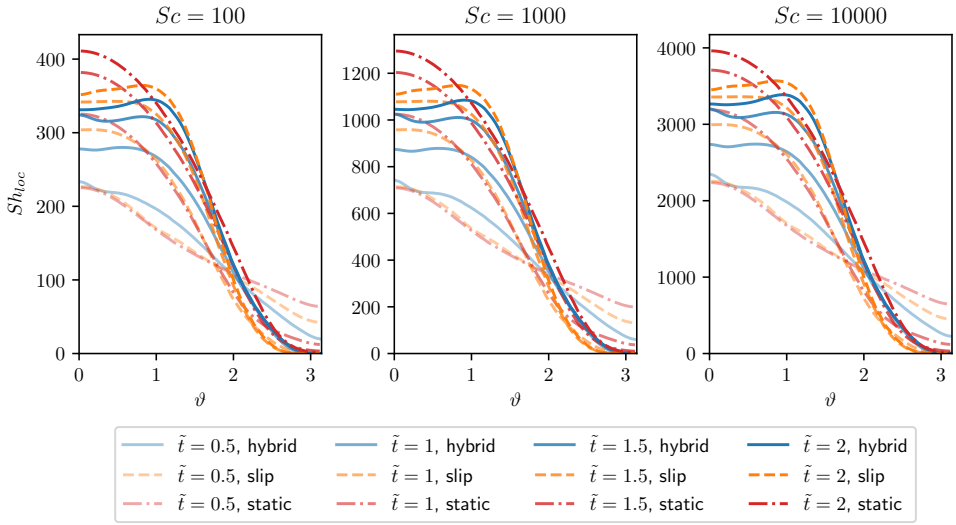

FIGURE 15 Local Sherwood number for test case 4 ($Re = 569$) computed with alternative boundary conditions at selected time instances in the transient phase.

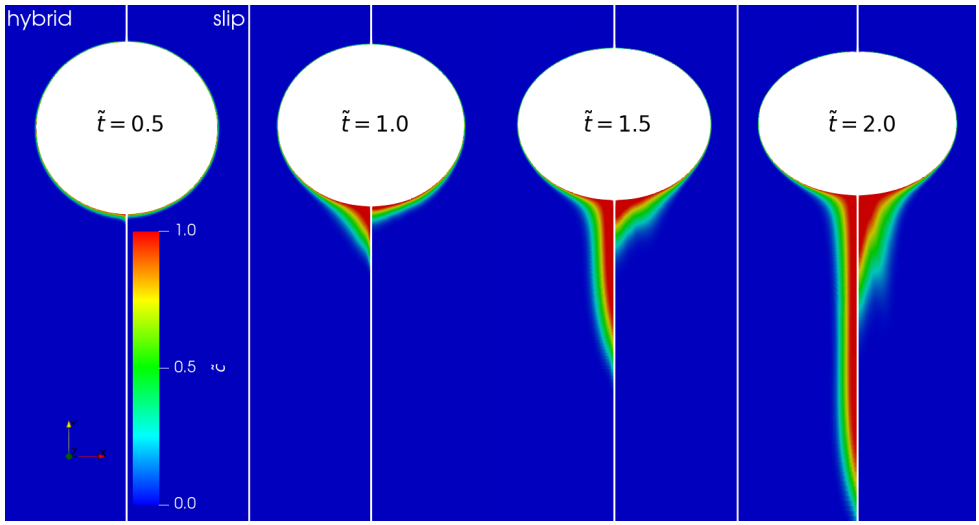

FIGURE 16 Concentration fields at selected time instances of test case 4 ($Re = 569$) computed with different boundary conditions for the interfacial velocity (left - hybrid, right - slip).

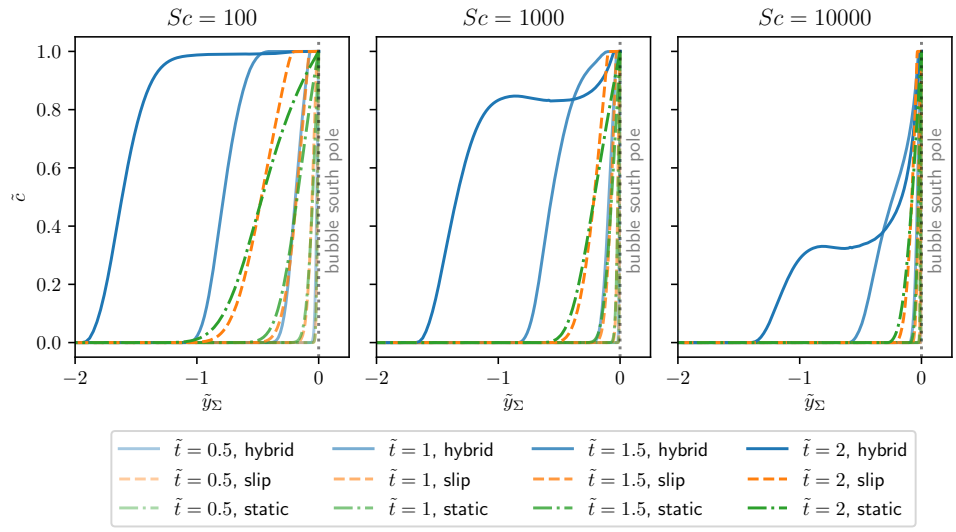

FIGURE 17 Concentration profiles along the y-axis at selected time instances of test case 4 ($Re = 569$) computed with alternative boundary conditions.

identifier	CB1	CB2	CB3	CB4
d_b in mm (water)	0.6	1.0	1.4	1.8
$Eo \times 10$	0.485	1.346	2.683	4.361
Ga	45.86	98.67	163.4	238.2
$\mu_l \times 10^3$ in $kg/(m \cdot s)$	21.81	10.13	6.118	4.197
σ in kg/s	20.64	7.429	3.790	2.293

TABLE 1 Investigated test cases in terms of Eo, Ga, the dynamic liquid viscosity μ_l, and the surface tension σ.

identifier	$\Delta \times 10^2$	d_b/Δ	$N_{cells}/10^3$
refinement 0	5.000	20	1104.5
refinement 1	3.125	32	4500
refinement 2	2.500	40	8836

TABLE 2 Characteristic mesh properties for mesh dependency study. The uniform cell width is denoted by Δ, and N_{cells} is the overall number of cells.

identifier	$\Delta_1 \times 10^4$	d_b/Δ_1	$N_{cells}/10^3$
refinement 0	5.00	2000	27
refinement 1	2.50	4000	108
refinement 2	1.25	8000	434

TABLE 3 Characteristic mesh properties for mesh dependency study. The width of the first cell layer normal to the bubble's surface is denoted by Δ_1, and N_{cells} is the overall number of cells. Note that Δ_1 undergoes small changes as the mesh deforms.

	Re_{sim}	χ_{sim}	Re_{Mei}	$Re_{Tomiyama}$	$\chi_{Duineveld}$
CB1	72	0.985	77	58	0.966
CB2	243	0.882	288	268	0.902
CB3	430	0.710	503	459	0.694
CB4	569	0.580	630	569	0.524

TABLE 4 Comparison of numerically obtained bubble Reynolds number and aspect ratio χ with reference data from literature. The reference aspect ratio was computed using a 4th-order polynomial fit of Duineveld's experimental data[43]. Note that the diameters of cases CB1 and CB2 are below the experimentally investigated diameter range in Duineveld et al.[43] and may contain some extrapolation error.